Jamming of nephron-forming niches in the developing mouse kidney creates cyclical mechanical stresses

Supplementary Information

Table of Contents

Supplementary Text

Supplementary Video Legends

Supplementary Video 1: Coordination of ureteric bud tip branching morphogenesis and nephron formation. Side-view schematic depicting four cycles of UB tip branching. UB tubules (green), cap mesenchyme (magenta), early nephrons (white). UB tips branch at the surface of the kidney and are surrounded by cap mesenchyme cell populations that repel each other. Early nephrons are induced at 'armpit' regions of tubules. Note that nephrons are distributed among daughter tips during each branching cycle. The movie represents the E15-19.5 period during which the tip branching rate matches the nephron formation rate[1]. Note the 'self-similar' nature of branching.

Supplementary Video 2: Asynchronous tip branching disrupts crystal-packed regions of tip domains *in silico*. (**A**) Conceptual movie of model tip domain pairs represented by sphere pairs repelling other pairs at an example E15 mouse kidney surface mesh. Tip domain pairs are added at random locations as the mesh grows isotropically such that tip domain number increases proportional to mesh surface area to the power 1.3 (ref. [2]). Spatial parameters over the course of the movie approximately reflect ~E15-E18. Note the emergence of square- and hexagonal close-packed regions that are disrupted spatially and temporally by tip branching events. (**B**) Inset of another simulation instance over the latter portion of (**A**) in which sphere pairs are shaded by relative local stress (proportional to elastic strain between pairs). Note local stress increases upon spatially random addition of new tip domain pairs.

Supplementary Video 3: Laser ablation causes rebound of cap mesenchyme and stroma between pairs of ureteric bud tips. Timelapse of E17 mouse embryonic kidney by widefield microscopy during laser microdissection (see **Methods**). The timelapse is played at ~10x real-time. UB tips are shown firstly by Alexa Fluor 488-PNA fluorescence. Ablation is then performed while imaging for all cells (CellTracker Red), and cut opening imaged for a further 45 s. The video concludes with a comparison of movie frames immediately after cutting vs. 45 s later.

Supplementary Notes

Supplementary Note 1. The hypothesis that nephron progenitor decision making and mechanical microenvironment are linked is motivated by the following observations: BMP/pSMAD and Wnt/β-catenin axes that prime and differentiate nephron progenitors are mechanosensitive in other contexts[3–5]. Nephron progenitor regulation is dependent on the mechanotransduction pathway member YAP[6–9], an integrator of mechanical cues affecting a range of differentiation events[6,7], and on appropriate Rho/ROCK and non-muscle myosin II activity[9–11]. The YAP pathway appeared as a branching life-cycle-correlated hit in nephron progenitor spatial sequencing[12]. Negative regulation of Rho GTPase, Rho-associated protein kinase (ROCK), and non-muscle myosin IIA/B isoforms (Myh9/Myh10) lead to increases in nephron formation (e.g. low dose H1152, a ROCK inhibitor) or decreases in nephron formation (e.g. high dose H1152; mesenchymal Myh9/Myh10 deletions)[9–11]. Both Rho/ROCK and non-muscle myosin IIA/B are important to cell tension and perception of the mechanical microenvironment[13,14]. Human stem-cell derived kidney organoid differentiation and nephron segment morphogenesis are sensitive to the mechanics of the encapsulating hydrogel[15]. Nephrogenesis is significantly increased during embryonic kidney explant culture under surface tension at an air-media interface, rather than suspended just below the media surface or in hanging drops[16]. Nephron formation in hemispherical bio-printed organoids is biased toward high-curvature edges[17], which are known to amplify mechanical strain[5].

Supplementary Note 2. Repulsive particles pack most efficiently on flat surfaces in a hexagonal close-packed (triangular lattice) fashion where each particle has six neighbors (i.e. the coordination number z = 6) (**Figure 1B**). However, this packing pattern cannot be maintained on a curved surface, since wrapping a triangular lattice onto a surface with non-zero Gaussian curvature creates strain[18]. This strain creates an energetic cost that favors the emergence of topological defects called disclinations, in which some particles have greater or fewer than six neighbors. For example, the strain introduced into a hexagonal lattice mapped onto a spherical surface can be relieved by introducing 12 pentagons (known as topological defects of 'charge' s = +1), such as in the familiar pattern of pentagons and hexagons making up a soccer ball. For curved crystals that are sufficiently large (R/a > 5 for spheres, where R is sphere radius and a is mean particle spacing), the energy cost of isolated pentagon (s = +1) defects becomes too large[19,20]. The resulting strain is therefore relieved through the spontaneous appearance of 'excess' dislocations as pairs, clusters, or chains of alternating charge (i.e. particles with coordination number 5-7-5-7-...-5) called 'grain boundary scars' each with a net charge of +1 that effectively distribute the elastic energy of the defect over a larger area[19,21,22].

Supplementary Note 3. The theory of curved crystals suggests that the amount of bias toward pentagon dislocations will increase linearly with curvature. This curvature dependence of tip geometry can be summarized by plotting total disclination defect charge Q for individual kidney fields of view against the surface integral of their Gaussian curvature (in units of disclinations), Ω. The Gauss-Bonnet theorem suggests that the overall topological charge will increase linearly here to "screen" curvature-induced stress[21,23].

Supplementary Note 4. Live imaging of cap mesenchyme cells in mouse kidney explants at an equivalent developmental time of ~E14 has shown their mean speed to be approximately 3.5 x 10^{-3} μm s^{-1} (12.6 μm hr^{-1}), compared to a relative divergence speed of sister UB tip domains of ~2-5 μm hr^{-1} (ref. [24]). Therefore, during early branching morphogenesis, cap reorganization is sufficient to consider it as a fluid-like compartment on the timescale of tip domain branching. Similarly, UB tips are dynamic and the tip domain actively remodels throughout the branching cycle via a 'lumenal mitosis' mechanism that drives cell dispersal[25]. Proliferating tip cells detach from the basement membrane, undergo mitosis within the tip lumen, and randomly reintegrate into nearby sites, fueling overall tip growth. Less is published on stromal cell dynamics, but for example endothelial cell induction from FOXD1+ stromal cells, recruitment, and reorganization into developing vascular plexuses at the border of tip domains is highly active during their branching[26].

Supplementary Note 5. Although ϕ predicts density-dependent jamming of niches, the underlying theory neglects potentially important parameters[27,28] including collective cell elasticity and active contractility (embryonic kidney cortex explants shrink in the hours after cutting[2]), and the contribution of cell-cell and cell-matrix adhesion to interfacial tension at cap-stroma interfaces. We therefore applied density-independent rigidity theory created for the high packing fraction regime that accounts for these parameters. Since niches pack side-to-side in one layer, we turned to a family of models developed for tissues organized into tessellated polygonal subunits having elasticity, contractility and interfacial tension[29–36]. This family includes 2D vertex models (where the degrees of freedom are the vertices of sub-unit polygons) and 2D Voronoi models (where the degrees of freedom are the Voronoi centers of sub-unit polygons). The vertex and Voronoi models are distinct, but in practice the local minimum energy states of the two are very similar[31]. Each model is based on forces imposed through the gradient of a dimensionless energy functional of the form[29–31,33–35,37]:

$$e = \sum_i [(P_i - P_0)^2 + k_A(A_i - 1)^2]$$

Where the average polygon area is 1, P_i is the actual perimeter of polygon i, P_0 is the preferred polygon perimeter, and A_i are actual polygon areas. k_A controls the relative area and perimeter moduli. The first term models contractility and interfacial tension. For cells, this would capture cell cytoskeletal contractility and cell-cell interfacial tension, while for tip domains this would capture collective cell contractility and domain-domain interfacial tension at the cap mesenchyme-stromal interfaces (**Figure 2B**). The second term models area elasticity. For cells, this would capture cell elasticity, while for tip domains this would capture collective cell elasticity. Rigidity transitions have been found in the 2D vertex model for $k_A = 0$ when the control parameter p_0 crosses a transition point at $p^*_0 = 3.87$, for $k_A > 0$ at $p^*_0 = 3.81\text{-}3.92$, and in the 2D Voronoi model for $k_A = 0$ at $p^*_0 = 3.82$ (ref. [29,34]). A strict rigidity transition does not occur in the 2D Voronoi model for $k_A > 0$, but it still exhibits a striking increase in e.g. elastic modulus in the vicinity of $p^*_0 = 3.8$ (ref. [33]). In practice we measure the median of the observed shape index, $\bar{p}$, an order parameter used as a proxy for p_0 (ref. [29,32]). We use p^* as short-hand for p^*_0 in the main text. This model family therefore identifies the shape index range of 3.8-3.92 as a threshold at which density-independent stiffening or a sharp rigidity transition may occur in tissues organized into tessellated polygonal sub-units such as cells or tip domains.

For tip domains, these energy terms are justified firstly by macroscopic behavior of embryonic kidney cortex explants, which actively contract and round up without loss of tip domain adhesion to neighbors in the hours after cutting[2]. Secondly, elasticity of tip domains is implied by positive stiffness values returned by microindentation on a length-scale appropriate to tip domain extents in xy and z (**Figure 3D**), and interfacial tensions are implied by rebound distances being positive in domain-domain interface ablation experiments (**Figure 5H**).

Supplementary Note 6. To draw a connection between tip domain shape index and our previous geometric model of tubule family packing[2], we produced heat maps of shape index for three characteristic tip packing regimes that appear in the model over developmental time. These regimes appear to exhibit amorphous, square-like, and hcp-like packing respectively, accounting for the reduction in shape index from E14-17 in both the model and kidney data (**Supplementary Figure 3A** and **Figure 2D**). In reality, tip packing does not perfectly adhere to any one regime at a snapshot in time (**Supplementary Figure 2H**, **Supplementary Figure 3B**). This could be caused by disruption of packed regions due to asynchronous tip branching that would displace neighbors (**Supplementary Video 2A**) and create heterogeneity (polydispersity) in the relative size and shape of tip domains. This means that our previous model predicts the stage at which a given packing phase may exist, but a mixture of phases arises in practice. For example, at mouse E17 and human week 18 we observe regions that exhibit amorphous, square-like, or hcp-like packing (**Supplementary Figure 2H**, **Supplementary Figure 3B**). These regions persist for 2-3 tip-to-tip spacings in xy, as revealed by spatial autocorrelation analysis showing four-fold and six-fold rotational symmetry for square-like and hcp-like regions respectively (**Supplementary Figure 3C**). Overall, these data show that tip domain

packing is semi-crystalline (having a mixture of amorphous and crystalline phases), with an increased prevalence of square- and hcp-packed regions predicted at later developmental times.

Supplementary Note 7. We verified that Brillouin shift correlated with polyacrylamide gel stiffness measured by microindentation (**Supplementary Figure 5**), adding to extensive validation data from hydrogels, cells, and tissues[38–40]. Although accurately translating the high-frequency Brillouin modulus to Young's modulus requires careful calibration specific to a given sample, we approximated the relative change in Young's modulus of cap mesenchyme based on an empirical log-log linear relationship established using cells[41]. For a Brillouin shift increase of 0.1 GHz, the relative increase in Young's modulus is ~46%.

Supplementary Note 8. Nephrons per tip domain can be scored from 3D confocal immunofluorescence stacks by summing counts of SIX2+ spheroids beneath UB tips (pre-tubular aggregate and renal vesicle stages) with counts of sites where connecting tubules from more mature nephrons connect to tips (comma shaped body, S-shaped body, and later stages), **Supplementary Figure 6A**. Any geometric parameter of tip domains can then serve as a suitable pseudotime metric in principle, so long as it 1) correlates with nephron number, 2) is relevant to branching progress, and 3) is measurable from imaging of fixed kidneys. In one such analysis we found a negative correlation between tip domain area and shape index, reflecting the proposed 'life-cycle' of tips. Recently divided tips bearing fewer nephrons had lower area and higher shape index, while older tips bearing more nephrons were larger with lower shape index (**Supplementary Figure 6B**). These data imply that the tip domain shape index can be used as a pseudotime metric to register tips with respect to their stage in the branching process (**Supplementary Figure 6C,D**). Calculating a rolling average of nephron number per tip over pseudotime revealed that nephrogenesis rate increases as the shape index of tip domains drops below an intermediate value of $p \sim 3.91$ (**Supplementary Figure 6E**). This means that nephrogenesis pauses as new tips branch outward against neighboring tip domains and begin to round up, and then resumes as tip domains then grow in area (**Supplementary Figure 7**).
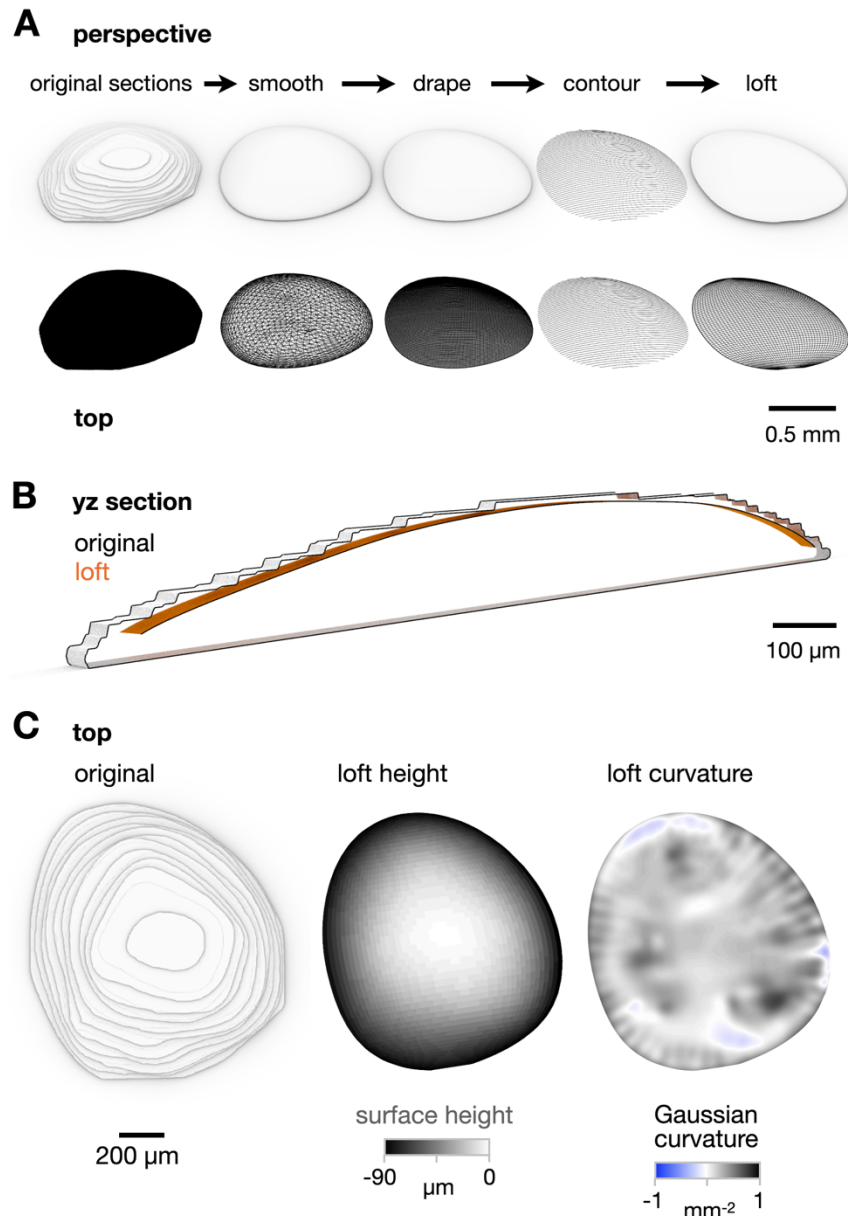
Supplementary Note 9. Cell nucleus elongation and alignment generally correlates with anisotropic stress and/or ECM fiber alignment[4,42–45]. Since there is no basement membrane at the cap mesenchyme-stromal interface and ECM fibers in mouse appear to be aligned along the corticomedullary (xz) axis rather than along ribbons in xy[46,47], we reasoned that any enrichment in nuclear elongation or alignment there would reflect local mechanical stresses[45].

Supplementary Note 10. We reasoned that force inference could be extended to the tissue level because both cells and tip domains can be modeled by networks of interfaces (cell junctions / stromal junctions) that transmit mechanical stress between neighbors. Bayesian force inference was applied according to a published procedure that assumes that tissues are in instantaneous mechanical equilibrium, tissue mechanics are dominated by in-plane tensions and pressures, and that interfacial tensions are positive[48,49]. Mechanical stresses can be determined from these data without assuming the biophysical origin or spatial localization of forces[48–51]. Force inference has been successfully validated by laser ablation experiments across several model organisms, tissue types, and length-scales (from several-cell to large multicellular tissues)[49]. The Bayesian approach is appropriate here, since it does not require measurement of interface curvatures, making it ideal for our application to large numbers of tip domains interfaces with negligible curvatures that can be closely approximated by polygonal Voronoi cell edges[49] (**Figure 1C,D**). Tensions and pressures are estimated from force balances at vertices of polygon junctions, where parallel (interfacial tension) and perpendicular (hydrostatic pressure, elasticity, and contractility) force contributions are transmitted to neighboring polygons. The biological origin of these forces may be distributed throughout polygons and need not be localized at junctions themselves[50,51]. Junctional stresses estimated through force inference are thought to be independent of other external contributions to total stress[49] due to e.g. out-of-plane basal interaction between tip domains and underlying cortical tissue.

Supplementary Note 11. Our data shows recoil velocities in the range of 0-8 μm min^{-1} and cut opening distances of 0-10 μm. Developmentally relevant recoil velocities are in the range of 1-60 μm min^{-1} for

cut opening distances of 0.4-8 µm in *Drosophila* amniosera, notum, retina, ventral furrow, and wing imaginal disk; the majority of these studies being at multi-cellular/tissue scale[49,52–57]. Perez-Gonzalez *et al.* saw recoil velocities of ~3-15 µm min^{-1} in mouse intestinal crypt organoids and used that to justify a force "dragging cells out of the crypt towards the villus…"[58]. Saha *et al.* analyzed recoil distances of < 2 µm in gastrulating zebrafish embryos[59], a site and time known for high morphogenetic forces. Kong *et al.* found cut opening distances of ~40 µm for tissue-scale cuts of ~400 µm length-scale (10% ratio) in quail embryos[49]. However, our maximum opening distances of ~10 µm are about as much as can be reasonably expected from cut lengths of ~40 µm (25% ratio), i.e. going from ⟺ to ⬯ in relative dimension. In the Saha *et al.* paper mentioned above, ~25 µm-length cuts go from ⟺ to ⬯. In other words, cut opening rates or dimensions cannot be significantly different from the cutting length-scale itself. These literature examples indicate that our recoil velocities and distances are consistent with those found in other multicellular morphogenesis events across diverse systems.

Supplementary Figures

A perspective

original sections → smooth → drape → contour → loft

top

0.5 mm

B yz section

original
loft

100 μm

C top

original

loft height

loft curvature

200 μm

surface height

-90 ──── 0
    μm

Gaussian
curvature

-1 ──── 1
   mm⁻²

Supplementary Figure 1: Kidney curvature analysis. (**A**) Perspective rendering (*top row*) and wireframes (*bottom row*) for example segmented E17 confocal stack and resulting surfaces generated after each processing step in Rhino (see **Methods**). (**B**) Mid-plane *yz* cross-sections of original segmented volume and loft surface after pre-processing steps, showing appropriate fit for subsequent curvature analysis. (**C**) Top (*xy*) view renderings of original volume, loft surface as a heatmap of height from MATLAB, and loft surface as a heatmap of Gaussian curvature from Rhino Grasshopper.
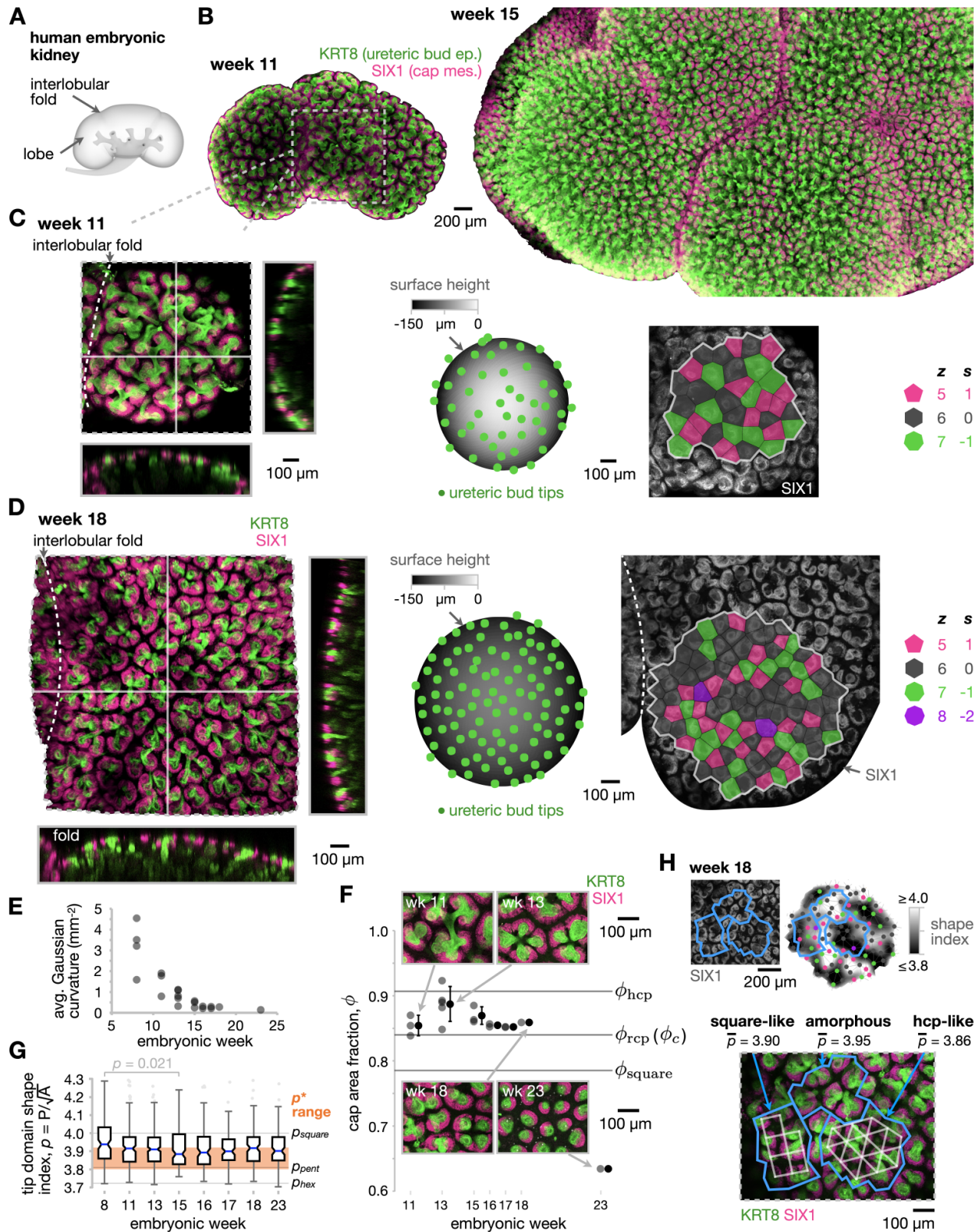
**Supplementary Figure 2: Human embryonic kidney tip domains show similar packing, shape index decrease over time, and semi-crystallinity as in mouse.** (**A**) Schematic of lobed human embryonic kidney. (**B**) Whole-mount confocal immunofluorescence maximum projections of week 11, 15 kidneys (data in (B)-(H) are a re-analysis of images published in ref. [60]). Markers are cytokeratin 8 (UB), SIX1 (nephron progenitors in cap mesenchyme). Caps are separated by ribbons of stroma (unlabeled). (**C**) *Left*, Detail and cross-sections of example week 11 lobe. *Middle*, UB tip positions overlaid on height map of the kidney surface. *Right*, Voronoi diagram tracing tip domains overlaid on SIX1 immunofluorescence channel. Voronoi cells are colored by coordination number (# neighbors). (**D**) The same elements for an example week 18 kidney lobe. (**E**) Average Gaussian curvature for patches of kidney lobe surface, *n* = 4, 3, 5, 3, 2, 2, 1, 1 patches across 4, 2, 3, 2, 1, 2, 1, 1

kidneys for week 8, 11, 13, 15, 16, 17, 18, 23 stages respectively. (**F**) Plot of cap mesenchyme area fraction ϕ over developmental time relative to 2D square packing, random close packing (rcp), and hexagonal close packing (hcp) of circles (mean ± S.D., *n* as for (**E**) except week 8 kidney SIX1 staining was not suitable to assess ϕ). (**G**) Box and whisker plots of tip domain shape index distributions over time, relative to those for squares, pentagons (*pent*), and hexagons (*hex*), and to $p^* = 3.8\text{-}3.92$ (*n* = 114, 168, 282, 144, 109, 102, 109, 104 tip domains across 4, 2, 3, 2, 1, 2, 1, 1 kidneys for week 8, 11, 13, 15, 16, 17, 18, 23 stages respectively. Unpaired two-tailed *t* test). Horizontal lines are minimum and maximum (excluding outliers), and quartiles (25/50/75%); points are outliers. (**H**) Representative case study of amorphous and crystalline (square-like, hcp-like) phases of tip domain packing at week 18. *Top*, Confocal micrograph of tip domains and shape index heatmap. Example packing regimes are outlined in blue. *Bottom*, Inset of these regions showing lattice lines and decreasing median shape index $\bar{p}$ from amorphous to square-like to hcp-like packing.
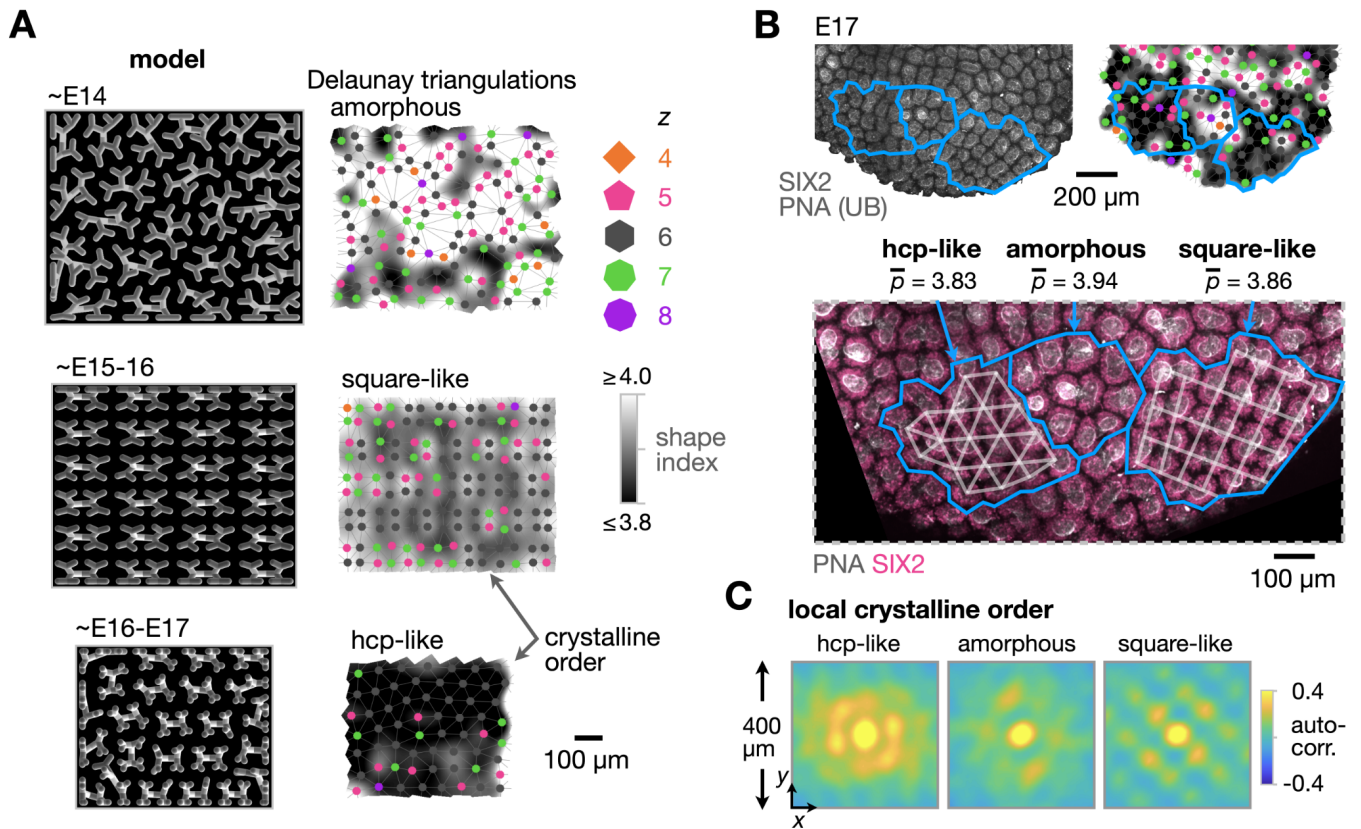
Supplementary Figure 3: Close packing of ureteric bud tip domains predicts emergence of semi-crystalline order over developmental time. (**A**) *Left column*, Representative physical model output for tubule packing regimes characteristic of the indicated developmental ranges, previously reported in ref. [2]. *Right column*, overlays of Delauney triangulations indicating coordination number of tip domains on spatial heatmaps of shape index, showing reducing shape index as tip patterns transition from amorphous to square-like to hcp-like regimes. (**B**) Representative case study of amorphous and crystalline (square-like, hcp-like) phases of tip domain packing at E17. *Top*, Confocal micrograph of tip domains and shape index heatmap. Example regions of different packing regimes are outlined in blue. *Bottom*, Inset of these regions showing lattice lines and decreasing median shape index $\bar{p}$ from amorphous to square-like to hcp-like packing. (**C**) Study of positional order within regions in (**B**) by spatial autocorrelation.
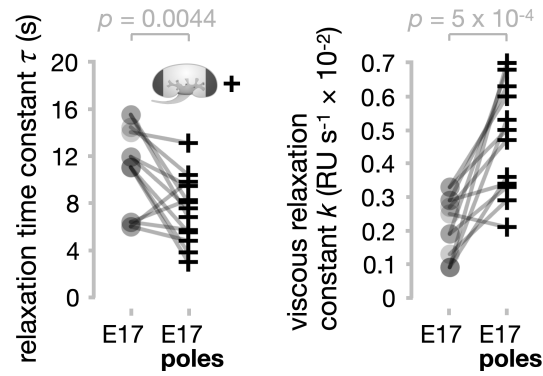
Supplementary Figure 4: E17 kidney pole regions have higher viscous relaxation than non-pole regions by microindentation. Plots of relaxation constants τ and k (see model sketch in **Figure 3B**) for paired measurements of E17 kidneys and their poles (n = 13, 12 measurement pairs for τ, k plots over 9 kidneys, 1-2 pairs per kidney, paired two-tailed t tests).

polyacrylamide gels
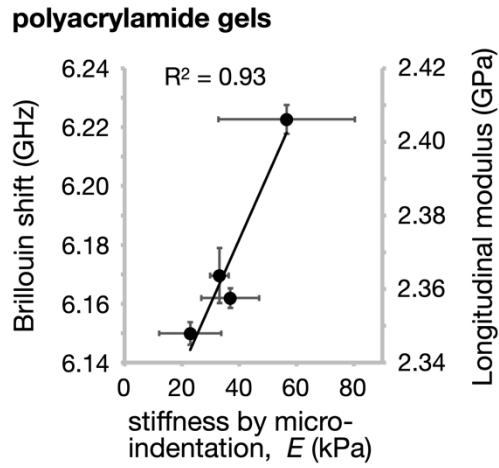
Supplementary Figure 5: Brillouin shift correlates with polyacrylamide gel stiffness measured by microindentation. Brillouin shift vs. stiffness by microindentation for 7.5% acrylamide/0.035, 0.05, 0.07, and 0.15% bis-acrylamide hydrogels, in order of microindentation stiffness (mean ± S.D., n = 6 and 3-8 measurements across 2 gels per composition for microindentation and Brillouin respectively).
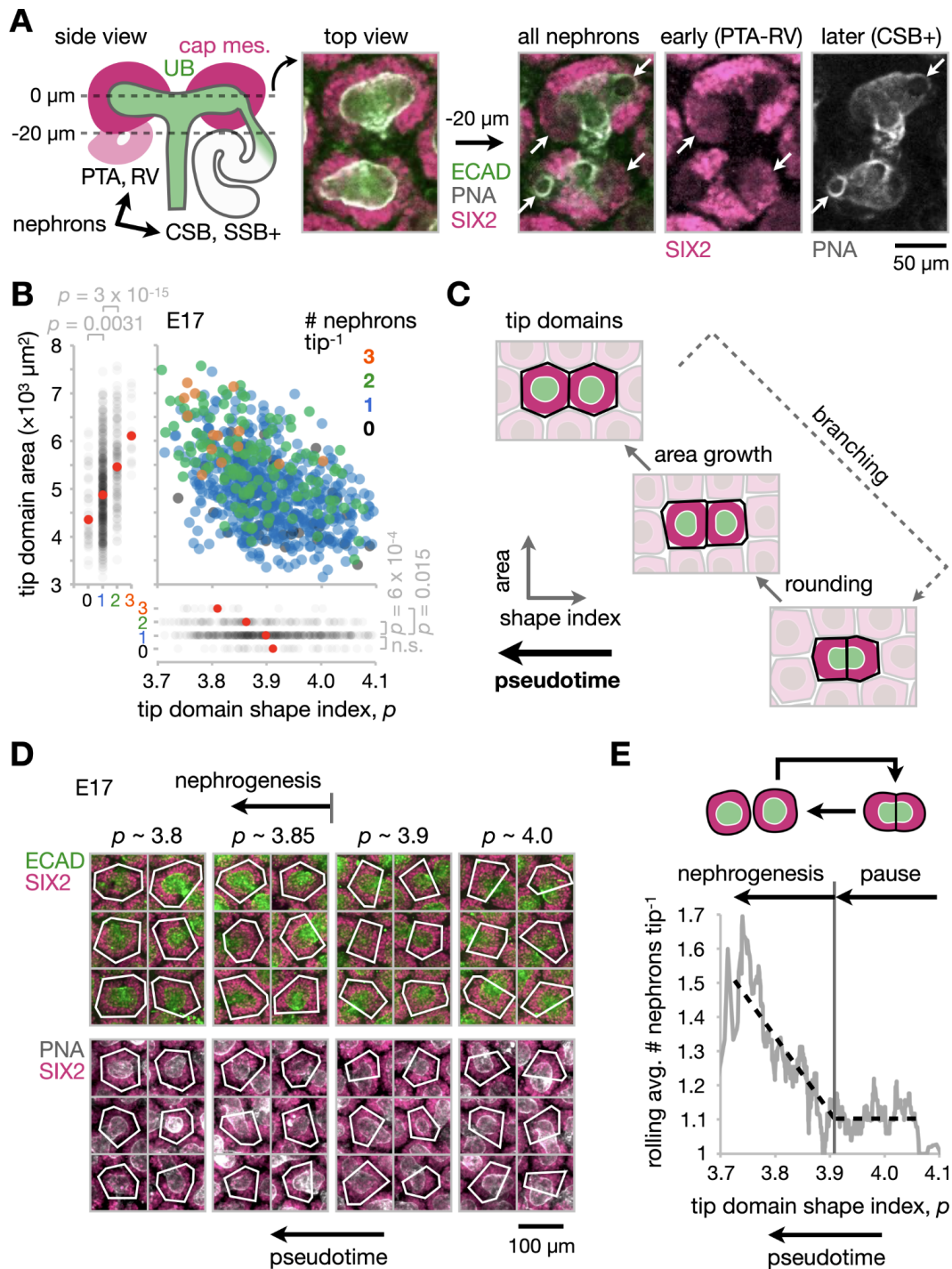
Supplementary Figure 6: Nephrogenesis rate varies over a tip domain 'life-cycle' defined by shape index.
(**A**) *Left*, Schematic showing side (*xz*) view of a pair of UB tips associated with early-stage nephrons (PTA, pre-tubular aggregate; RV, renal vesicle) and later-stage nephrons (CSB, comma shaped body; SSB, S-shaped body). *Right*,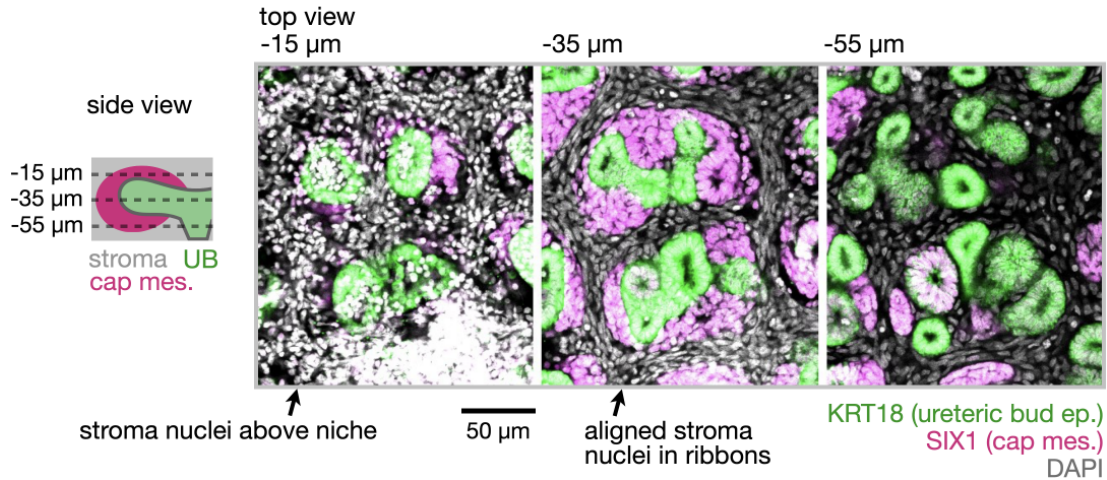 Top-view confocal immunofluorescence micrographs at the mid-plane of UB tips and 20 μm deeper into an E17 kidney. All nephrons associated with each tip can be annotated either as SIX2+ spheroids for early nephrons or from the attachment points of their connecting tubules for later nephrons (white circles at tips in PNA channel), see arrows. (**B**) Plot of tip domain area against shape index, with nephron number per tip in the color dimension (*n* = 42, 494, 133, 15 tip domains for 0, 1, 2, 3 nephron # per tip categories across 4 E17 kidneys. One-way ANOVA, Tukey's test). Each axis is also plotted individually vs. nephron number per tip. (**C**) Schematic of UB tip life-cycle and definition of a pseudotime based on shape index of tip domains. (**D**) Example confocal micrographs of tip domains over a range in shape index. (**E**) Rolling average of nephron number per tip against shape index (window width = 50 points).
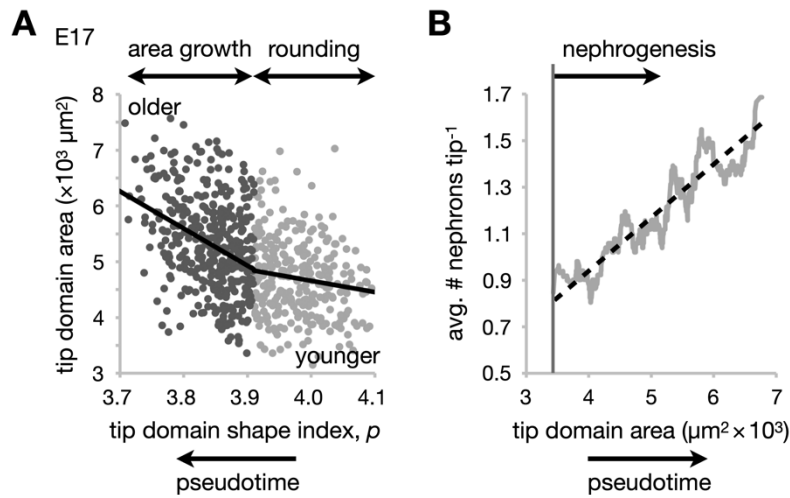
Supplementary Figure 7: Tip domains transition from rounding-dominated to area growth-dominated regimes over tip life-cycle. (**A**) A version of **Supplementary Figure 6B** divided into two periods during the tip life-cycle before (right side) and after (left side) nephrogenesis begins (**Supplementary Figure 6E**). Note that younger tip domains with fewer nephrons primarily round up prior to the nephrogenesis phase, which then coincides with a higher rate of tip domain area increase. (**B**) A version of **Supplementary Figure 6E** except plotted against tip domain area rather than shape index.

human embryonic kidney, week 17

top view
-15 μm   -35 μm   -55 μm

side view

-15 μm
-35 μm
-55 μm

stroma UB
cap mes.

stroma nuclei above niche   50 μm   aligned stroma
nuclei in ribbons

KRT18 (ureteric bud ep.)
SIX1 (cap mes.)
DAPI

Supplementary Figure 8: Cortical stromal cells align along tip domain interfaces in human embryonic kidney. *Left*, schematic of niche structure and positions of optical sections. *Right*, Whole-mount confocal immunofluorescence sections of a representative group of 4 UB tip domains at three section depths as indicated at left. Image data are a re-analysis of confocal stacks published in ref. [60]).
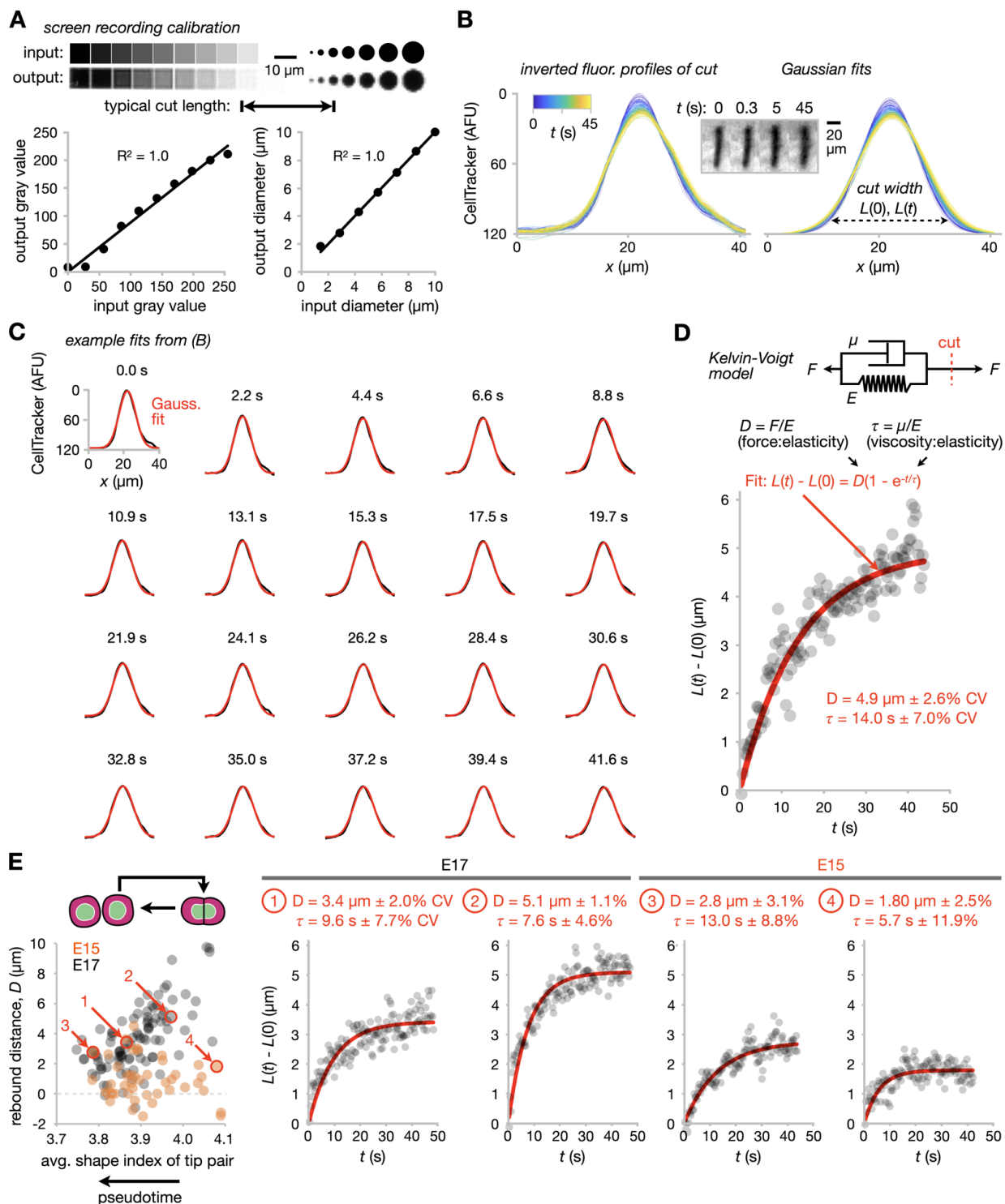
Supplementary Figure 9: Kidney cortex ablation data fits standard Kelvin-Voigt model of cut retraction with sufficient temporal and spatial resolution. (**A**) Intensity and spatial calibration target patterns and plots from ablation instrument screen to iPhone-based data readout. Output diameter was estimated by manual segmentation. (**B**) Inverted fluorescence profiles, *left*, and Gaussian fits, *right*, for an example cut over time, *inset*. (**C**) Individual overlays of inverted cut fluorescence and Gaussian fit at a sub-sample of movie frames. (**D**) *Top*, Schematic of Kelvin-Voigt model (spring and dashpot in parallel) for cut opening, having asymptotic cut opening distance D and single-exponential opening dynamics captured by the time constant τ. D reports on force:elasticity ratio in the tissue prior to the cut being made[61,62]. *Bottom*, Cut fluorescence is Gaussian fit for each movie frame, plotted as cut width $L(t)$-$L(0)$ at 10% of maximum vs. time, and fit with the Kelvin-Voigt model equation. Fit parameters and coefficients of variation are indicated. (**E**) Cut opening distance trajectories for example cuts from E15 and E17 kidneys analyzed in **Figure 5H**, showing sufficient temporal resolution and spatial accuracy for model fitting within reasonable error thresholds (error estimates of D and τ were <5% and <15% coefficient of variation respectively).

Supplementary Figure 10: Laser ablation case studies over the niche life-cycle. Example laser ablation cases for 15 cuts on E17 kidneys. Representative cases are displayed for average shape index of the tip domains immediately adjacent to each cut in the vicinity of p ~ 3.8, 3.9, and 4.0 to visually contrast cut opening magnitudes among these categories. Each case shows fluorescence micrographs of UB tips with cut ROIs and local Voronoi diagram overlaid, and kidney surface fluorescence immediately after cutting and after 45 s. Cut boundaries and associated rebound distances are also shown. White arrows indicate the cut of interest if more than one cut appears in the field of view. *Inset*, zooming in to show boundaries for a representative subset of cuts, note higher rebound distances for cuts made between younger niches having higher average shape index that are earlier in their branch life-cycles.

Supplementary References

1. Short, K. M. *et al.* Global quantification of tissue dynamics in the developing mouse kidney. *Dev. Cell* **29**, 188–202 (2014).
2. Prahl, L. S., Viola, J. M., Liu, J. & Hughes, A. J. The developing murine kidney actively negotiates geometric packing conflicts to avoid defects. *Dev. Cell* **58**, 110-120.e5 (2023).
3. Shyer, A. E. *et al.* Emergent cellular self-organization and mechanosensation initiate follicle pattern in the avian skin. *Science* **357**, 811–815 (2017).
4. Parada, C. *et al.* Mechanical feedback defines organizing centers to drive digit emergence. *Dev. Cell* **57**, 854-866.e6 (2022).
5. Muncie, J. M. *et al.* Mechanical tension promotes formation of gastrulation-like nodes and patterns mesoderm specification in human embryonic stem cells. *Dev. Cell* **55**, 679-694.e11 (2020).
6. Panciera, T., Azzolin, L., Cordenonsi, M. & Piccolo, S. Mechanobiology of YAP and TAZ in physiology and disease. *Nat. Rev. Mol. Cell Biol.* **18**, 758–770 (2017).
7. Dupont, S. *et al.* Role of YAP/TAZ in mechanotransduction. *Nature* **474**, 179–183 (2011).
8. Reginensi, A. *et al.* Yap- and Cdc42-dependent nephrogenesis and morphogenesis during mouse kidney development. *PLoS Genet.* **9**, e1003380 (2013).
9. Tanigawa, S., Sharma, N., Hall, M. D., Nishinakamura, R. & Perantoni, A. O. Preferential propagation of competent SIX2+ nephronic progenitors by LIF/ROCKi treatment of the metanephric mesenchyme. *Stem Cell Reports* **5**, 435–447 (2015).
10. Lindström, N. O., Hohenstein, P. & Davies, J. A. Nephrons require Rho-kinase for proximal-distal polarity development. *Sci. Rep.* **3**, 2692 (2013).
11. Recuenco, M. C. *et al.* Nonmuscle myosin II regulates the morphogenesis of metanephric mesenchyme-derived immature nephrons. *J. Am. Soc. Nephrol.* **26**, 1081–1091 (2015).
12. Davis, S. N. *et al.* Nephron progenitors rhythmically alternate between renewal and differentiation phases that synchronize with kidney branching morphogenesis. *bioRxiv* (2023) doi:10.1101/2023.11.21.568157.
13. Janmey, P. A., Wells, R. G., Assoian, R. K. & McCulloch, C. A. From tissue mechanics to transcription factors. *Differentiation* **86**, 112–120 (2013).
14. Muncie, J. M. & Weaver, V. M. The physical and biochemical properties of the extracellular matrix regulate cell fate. *Curr. Top. Dev. Biol.* **130**, 1–37 (2018).
15. Nerger, B. A. *et al.* 3D hydrogel encapsulation regulates nephrogenesis in kidney organoids. *Adv. Mater.* **36**, e2308325 (2024).
16. Sebinger, D. D. R. *et al.* A novel, low-volume method for organ culture of embryonic kidneys that allows development of cortico-medullary anatomical organization. *PLoS One* **5**, e10550 (2010).
17. Lawlor, K. T. *et al.* Cellular extrusion bioprinting improves kidney organoid reproducibility and conformation. *Nat. Mater.* **20**, 260–271 (2021).
18. Manoharan, V. N. COLLOIDS. Colloidal matter: Packing, geometry, and entropy. *Science* **349**, 1253751 (2015).
19. Bausch, A. R. *et al.* Grain boundary scars and spherical crystallography. *Science* **299**, 1716–1718 (2003).
20. Bowick, M. J., Nelson, D. R. & Travesset, A. Interacting topological defects on frozen topographies. *Phys. Rev. B Condens. Matter* **62**, 8738–8751 (2000).
21. Irvine, W. T. M., Vitelli, V. & Chaikin, P. M. Pleats in crystals on curved surfaces. *Nature* **468**, 947–951 (2010).
22. Brojan, M., Terwagne, D., Lagrange, R. & Reis, P. M. Wrinkling crystallography on spherical surfaces. *Proc. Natl. Acad. Sci. U. S. A.* **112**, 14–19 (2015).
23. Jiménez, F. L., Stoop, N., Lagrange, R., Dunkel, J. & Reis, P. M. Curvature-controlled defect localization in elastic surface crystals. *Phys. Rev. Lett.* **116**, 104301 (2016).
24. Combes, A. N., Lefevre, J. G., Wilson, S., Hamilton, N. A. & Little, M. H. Cap mesenchyme cell swarming during kidney development is influenced by attraction, repulsion, and adhesion to the ureteric tip. *Dev. Biol.* **418**, 297–306 (2016).
25. Packard, A. *et al.* Luminal mitosis drives epithelial cell dispersal within the branching ureteric bud. *Dev. Cell* **27**, 319–330 (2013).
26. Munro, D. A. D., Hohenstein, P. & Davies, J. A. Cycles of vascular plexus formation within the

nephrogenic zone of the developing mouse kidney. *Sci. Rep.* **7**, (2017).

27. Bi, D., Lopez, J. H., Schwarz, J. M. & Manning, M. L. Energy barriers and cell migration in densely packed tissues. *Soft Matter* **10**, 1885–1890 (2014).
28. Mason, T. G., Bibette, J. & Weitz, D. A. Yielding and flow of monodisperse emulsions. *J. Colloid Interface Sci.* **179**, 439–448 (1996).
29. Bi, D., Lopez, J. H., Schwarz, J. M. & Manning, M. L. A density-independent rigidity transition in biological tissues. *Nat. Phys.* **11**, 1074–1079 (2015).
30. Farhadifar, R., Röper, J.-C., Aigouy, B., Eaton, S. & Jülicher, F. The influence of cell mechanics, cell-cell interactions, and proliferation on epithelial packing. *Curr. Biol.* **17**, 2095–2104 (2007).
31. Bi, D., Yang, X., Marchetti, M. C. & Manning, M. L. Motility-driven glass and jamming transitions in biological tissues. *Phys. Rev. X.* **6**, (2016).
32. Park, J.-A. *et al.* Unjamming and cell shape in the asthmatic airway epithelium. *Nat. Mater.* **14**, 1040–1048 (2015).
33. Sussman, D. M. & Merkel, M. No unjamming transition in a Voronoi model of biological tissue. *Soft Matter* **14**, 3397–3403 (2018).
34. Merkel, M., Baumgarten, K., Tighe, B. P. & Manning, M. L. A minimal-length approach unifies rigidity in underconstrained materials. *Proc. Natl. Acad. Sci. U. S. A.* **116**, 6560–6568 (2019).
35. Nagai, T. & Honda, H. A dynamic cell model for the formation of epithelial tissues. *Philos. Mag. B* **81**, 699–719 (2001).
36. Morse, P. K. & Corwin, E. I. Geometric order parameters derived from the Voronoi tessellation show signatures of the jamming transition. *Soft Matter* **12**, 1248–1255 (2016).
37. Staple, D. B. *et al.* Mechanics and remodelling of cell packings in epithelia. *Eur. Phys. J. E Soft Matter* **33**, 117–127 (2010).
38. Scarcelli, G. *et al.* Noncontact three-dimensional mapping of intracellular hydromechanical properties by Brillouin microscopy. *Nat. Methods* **12**, 1132–1134 (2015).
39. Scarcelli, G., Kim, P. & Yun, S. H. In vivo measurement of age-related stiffening in the crystalline lens by Brillouin optical microscopy. *Biophys. J.* **101**, 1539–1545 (2011).
40. Zhang, J., Nikolic, M., Tanner, K. & Scarcelli, G. Rapid biomechanical imaging at low irradiation level via dual line-scanning Brillouin microscopy. *Nat. Methods* **20**, 677–681 (2023).
41. Zhang, J. *et al.* Nuclear mechanics: Nuclear mechanics within intact cells is regulated by cytoskeletal network and internal nanostructures (small 18/2020). *Small* **16**, 2070098 (2020).
42. Alisafaei, F., Jokhun, D. S., Shivashankar, G. V. & Shenoy, V. B. Regulation of nuclear architecture, mechanics, and nucleocytoplasmic shuttling of epigenetic factors by cell geometric constraints. *Proc. Natl. Acad. Sci. U. S. A.* **116**, 13200–13209 (2019).
43. Versaevel, M., Grevesse, T. & Gabriele, S. Spatial coordination between cell and nuclear shape within micropatterned endothelial cells. *Nat. Commun.* **3**, 671 (2012).
44. Brownfield, D. G. *et al.* Patterned collagen fibers orient branching mammary epithelium through distinct signaling modules. *Curr. Biol.* **23**, 703–709 (2013).
45. Fernández, P. A. *et al.* Surface-tension-induced budding drives alveologenesis in human mammary gland organoids. *Nat. Phys.* **17**, 1130–1136 (2021).
46. Lipp, S. N., Jacobson, K. R., Hains, D. S., Schwarderer, A. L. & Calve, S. 3D Mapping Reveals a Complex and Transient Interstitial Matrix During Murine Kidney Development. *J. Am. Soc. Nephrol.* **32**, 1649–1665 (2021).
47. Lipp, S. N., Jacobson, K. R., Schwaderer, A. L., Hains, D. S. & Calve, S. FOXD1 is required for 3D patterning of the kidney interstitial matrix. *Dev. Dyn.* **252**, 463–482 (2023).
48. Ishihara, S. & Sugimura, K. Bayesian inference of force dynamics during morphogenesis. *J. Theor. Biol.* **313**, 201–211 (2012).
49. Kong, W. *et al.* Experimental validation of force inference in epithelia from cell to tissue scale. *Sci. Rep.* **9**, 14647 (2019).
50. Guirao, B. *et al.* Unified quantitative characterization of epithelial tissue development. *Elife* **4**, (2015).
51. Sugimura, K., Lenne, P.-F. & Graner, F. Measuring forces and stresses in situ in living tissues. *Development* **143**, 186–196 (2016).
52. Rauzi, M., Verant, P., Lecuit, T. & Lenne, P.-F. Nature and anisotropy of cortical forces orienting Drosophila tissue morphogenesis. *Nat. Cell Biol.* **10**, 1401–1410 (2008).

53. Bonnet, I. *et al.* Mechanical state, material properties and continuous description of an epithelial tissue. *J. R. Soc. Interface* **9**, 2614–2623 (2012).
54. Ma, X., Lynch, H. E., Scully, P. C. & Hutson, M. S. Probing embryonic tissue mechanics with laser hole drilling. *Phys. Biol.* **6**, 036004 (2009).
55. Martin, A. C., Gelbart, M., Fernandez-Gonzalez, R., Kaschube, M. & Wieschaus, E. F. Integration of contractile forces during tissue invagination. *J. Cell Biol.* **188**, 735–749 (2010).
56. Etournay, R. *et al.* Interplay of cell dynamics and epithelial tension during morphogenesis of the Drosophila pupal wing. *Elife* **4**, e07090 (2015).
57. Saias, L. *et al.* Decrease in cell volume generates contractile forces driving dorsal closure. *Dev. Cell* **33**, 611–621 (2015).
58. Pérez-González, C. *et al.* Mechanical compartmentalization of the intestinal organoid enables crypt folding and collective cell migration. *Nat. Cell Biol.* **23**, 745–757 (2021).
59. Saha, A. *et al.* Determining physical properties of the cell cortex. *Biophys. J.* **110**, 1421–1429 (2016).
60. Lindström, N. O. *et al.* Conserved and divergent features of human and mouse kidney organogenesis. *J. Am. Soc. Nephrol.* **29**, 785–805 (2018).
61. Zulueta-Coarasa, T. & Fernandez-Gonzalez, R. Laser ablation to investigate cell and tissue mechanics in vivo. in *Integrative Mechanobiology* (eds. Sun, Y., Kim, D.-H. & Simmons, C. A.) 128–147 (Cambridge University Press, Cambridge, 2015).
62. Rauzi, M. & Lenne, P.-F. Cortical forces in cell shape changes and tissue morphogenesis. *Curr. Top. Dev. Biol.* **95**, 93–144 (2011).